Photonic integrated filter with widely tunable bandwidth

Piero Orlandi, Francesco Morichetti, Michael John Strain, *Member, IEEE,* Marc Sorel, *Member, IEEE,* Paolo Bassi, *Member, OSA,* and Andrea Melloni

***Abstract*—We present a comprehensive design, fabrication and characterization analysis of compact silicon-on-insulator bandpass filters with widely tunable bandwidth. The filter architecture is based on an unbalanced Mach-Zehnder interferometer loaded with a pair of ring resonators. A wide bandwidth tunability (from 10% to 90% FSR) can be achieved by controlling the resonant frequency of the rings while preserving a good filter off-band rejection. Design rules are provided that take into account fabrication tolerances as well as losses. Further, the use of tunable couplers allows a more flexible shaping of the spectral response of the filter. The sensitivity with respect to nonlinear effects is carefully investigated. Operation over a wavelength spectrum of 20 nm is demonstrated, making the device suitable for channel subset selection in WDM systems, reconfigurable filters for gridless networking and adaptive filtering of signals.**

***Index Terms*—Bandpass filters, integrated optics, optical waveguide components, silicon on insulator technology.**

I. Introduction

PHOTONIC integrated circuits able to reconfigure and adapt their characteristics to the system requirements are becoming increasingly important in many applications including on-chip networking [1], [2], microwave photonics [3]–[5] and optical communication systems [6]. In this scenario, reconfigurable filters play a key role in the development of highly functional modules to meet the required system flexibility. Beside technical features, cost issue and compatibility with standard Integrated Circuits fabrication techniques must be also considered. This fostered the silicon photonics platform as the most promising technological fabrication approach. Photonic integrated filters design has been deeply investigated and many different techniques have been proposed for the synthesis of the desired filter response [7]–[10]. However, the capability to tune both the filter bandwidth and the filter central wavelength is not straightforward. For example single resonators with tuning of their coupling sections [11], [12] offer limited bandwidth tunability range or poor off-band rejection. By embedding ring resonators (RRs) in an unbalanced Mach-Zehnder Interferometer (MZI) it is possible to improve the filter performance [13], [14]. The use of RRs in add drop configuration [13] can bring to a limited bandwidth tuning range due to in-band ripples and insertion loss despite high off-band rejection values. Better design flexibility, bandwidth tunability, high off-band rejection and simple control can be obtained using several all pass RRs [14]. All pass RRs combined with MZI have also been used as unit cell of cascaded filters with two [15] or more stages [3] to allow a wide tunability of the filter characteristics. To achieve the described performance a large number of actuators to control the phases and the coupling coefficients of the RRs and of the MZI is however required. We recently proposed a simpler solution based on three actuators where wide bandwidth tunability can be achieved preserving a good off-band rejection for all the filter configurations [16].

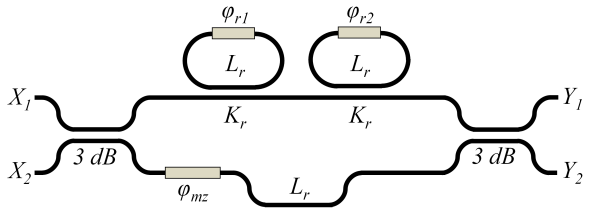

Fig. 1. Schematic diagram of the tunable filter architecture.

In this work we provide an extended analysis of the filter design and functionality as well as the demonstration of improved flexibility through the realization of two tunable coupling sections for the all pass RRs. The simultaneous and correct tuning of many passbands and the filter robustness against nonlinear effects is also investigated. All these features make the device suitable for channel subset selection in WDM systems, reconfigurable filters for gridless networking and adaptive filtering of signals.

The paper is structured as follows. In Section II the device functionality is illustrated through the Z transform formalism. In Section III the filter performance are investigated providing a tool for the design. In Section IV group delay and dispersion are discussed in relation to the filter design. Section V shows the realized devices performance and in Section VI the full control over the device functionality is demonstrated through the realization of tunable coupling sections for the RRs. In section VII the simultaneous and correct passband tuning over several device FSR is analyzed. In Section VIII we demonstrate the robustness of the proposed device against non linear two-photon absorption (TPA)/free carrier absorption (FCA) induced thermal effects. Finally, in Section X, the

P. Orlandi and P. Bassi are with the Dipartimento di Ingegneria dell'Energia Elettrica e dell'Informazione, Università di Bologna, Bologna 40136, Italy (e-mail: piero.orlandi@unibo.it; paolo.bassi@unibo.it).

F. Morichetti and A. Melloni are with the Dipartimento di Elettronica, Informazione e Bioingegneria, Politecnico di Milano, Milano 20133, Italy (e-mail: morichetti@elet.polimi.it; melloni@elet.polimi.it).

M.J. Strain and M. Sorel are with the School of Engineering, University of Glasgow, Glasgow G12 8LT, U.K. (e-mail: Michael.Strain@glasgow.ac.uk; Marc.Sorel@glasgow.ac.uk).

conclusions are drawn.

II. Filter Functionality

The filter architecture is shown in Fig. 1. It is based on an asymmetric Mach-Zehnder Interferometer (MZI) with 3 dB input and output couplers. Two racetrack resonators (RRs) in all pass configuration with the same geometric length L_r and power coupling coefficient K_r load one of the MZI arms. The length of the unloaded arm is set to have an optical path difference equal to L_r so that the Free Spectral Range (FSR) of the RRs matches that of the MZI.

Bandwidth tunability is achieved by controlling the three phase shifters represented by the gray boxes in Fig. 1. The tuning of the RRs phase difference $\Delta\varphi = \varphi_{r2} - \varphi_{r1}$ allows the control of the filter 3 dB bandwidth while the condition $\varphi_{mz} = m\pi + (\varphi_{r1} + \varphi_{r2})/2$ with m integer allows a filter transfer function always symmetric with respect to the filter central frequency f_0.

The spectral response of the device can be described through the Z transform approach [17] as

$$\begin{bmatrix} Y_1 \\ Y_2 \end{bmatrix} = \begin{bmatrix} H_{11}(z) & H_{12}(z) \\ H_{21}(z) & H_{22}(z) \end{bmatrix} \begin{bmatrix} X_1 \\ X_2 \end{bmatrix} =$$

$$= \begin{bmatrix} \frac{1}{\sqrt{2}} & -j\frac{1}{\sqrt{2}} \\ -j\frac{1}{\sqrt{2}} & \frac{1}{\sqrt{2}} \end{bmatrix} \begin{bmatrix} H_R(z) & 0 \\ 0 & \gamma e^{-j\varphi_{mz}} z^{-1} \end{bmatrix} \times$$

$$\times \begin{bmatrix} \frac{1}{\sqrt{2}} & -j\frac{1}{\sqrt{2}} \\ -j\frac{1}{\sqrt{2}} & \frac{1}{\sqrt{2}} \end{bmatrix} \begin{bmatrix} X_1 \\ X_2 \end{bmatrix}, \tag{1}$$

where X_i and Y_i $(i = 1, 2)$ represent respectively the complex amplitudes of the optical fields at the input and at the output of the system. In the following of the paper $X_1 = 1$ and $X_2 = 0$ will be assumed. It holds $z^{-1} = e^{-j2\pi fT}$, where f represents the optical frequency and T is the unit delay. This delay is given by $T = (n_g L_r/c) = (1/\text{FSR})$, where n_g is the waveguide group index and c the speed of light in vacuum. $H_R(z)$ represents the RRs cascade transfer function and can be expressed as

$$H_R(z) = \prod_{i=1}^{2} \frac{a e^{-j\varphi_{ri}} (\rho e^{j\varphi_{ri}} - a\gamma z^{-1})}{(1 - \rho a\gamma e^{-j\varphi_{ri}} z^{-1})}, \tag{2}$$

where $\rho = \sqrt{1 - K_r}$ is the coupler field transmission coefficient and a is the coupler loss factor. Moreover, γ is the field propagation loss factor associated to a propagation length L_r. The ring resonator round trip loss factor is then defined by the product $a\gamma = \gamma_r$. Using (1) and (2) the through and the cross port transfer functions ($H_{11}(z)$ and $H_{21}(z)$) can be expressed as the ratio between two third order polynomials $N(z)$ and $D(z)$ as

$$H_{11}(z) = \frac{1}{2} \cdot \frac{N_{11}(z)}{D_{11}(z)}, \tag{3}$$

$$H_{21}(z) = -\frac{j}{2} \cdot \frac{N_{21}(z)}{D_{21}(z)}. \tag{4}$$

These two equations account for the behaviour of a general filter. Its key parameters (3 dB bandwidth, off-band rejection and shape factor), besides $\Delta\varphi$, depend also on the coupling coefficient ρ (or K_r) and the loss factors a and γ. To rapidly highlight how $\Delta\varphi$ influences the system poles and zeros location and consequently the filter performance, a lossless device can be considered (i.e. $a = \gamma = 1$) with a given value of K_r. Using (1) and (2) it is thus possible to write:

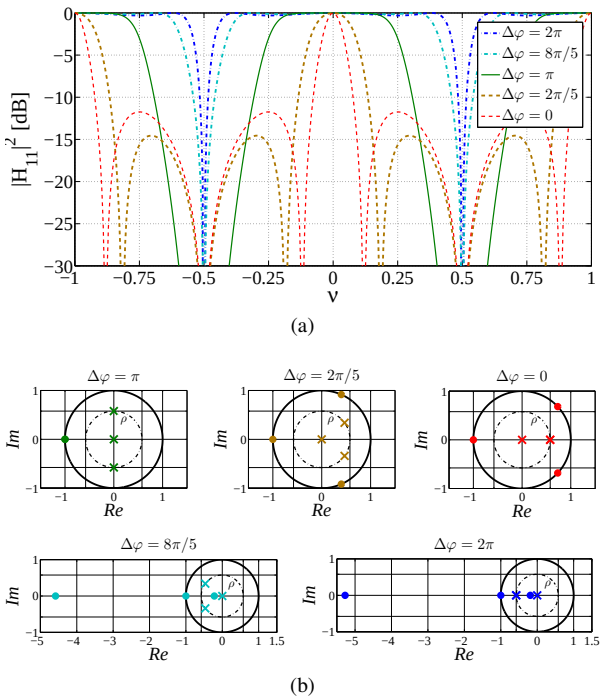

Fig. 2. (Color online) (a) Filter through port intensity transmission for $K_r = 2/3$ (i.e. $\rho = 1/\sqrt{3}$) and different $\Delta\varphi$ as a function of the normalized frequency $\nu = (f - f_0)/\text{FSR}$. (b) Relative pole-zero diagrams where poles and zeroes are represented respectively by crosses and dots.

$$\begin{aligned} N_{11}(z) =& \rho^2 + [1 - 2\rho\cos(\Delta\varphi/2)]\, z^{-1} \\ &+ [1 - 2\rho\cos(\Delta\varphi/2)]\, z^{-2} \\ &+ \rho^2 z^{-3}, \end{aligned} \tag{5}$$

$$\begin{aligned} N_{21}(z) =& \rho^2 - [1 + 2\rho\cos(\Delta\varphi/2)]\, z^{-1} \\ &+ [1 + 2\rho\cos(\Delta\varphi/2)]\, z^{-2} \\ &- \rho^2 z^{-3} \end{aligned} \tag{6}$$

and

$$D_{11}(z) = D_{21}(z) = 1 - 2\rho\cos(\Delta\varphi/2) z^{-1} + \rho^2 z^{-2}. \tag{7}$$

where $\varphi_{r2} = -\varphi_{r1} = \varphi_r$ and $\varphi_{mz} = \pi$ has been considered to simplify the notation without lack of generality. In fact adding a phase φ_0 to the three phases produces just a rigid shift of the filter characteristic while a π variation of φ_{mz} produces just a swap between the through and cross port transfer functions. Moreover to analyse the filter response, it is more convenient to consider the complex variable z^{-1} as a function of the normalized frequency $\nu = (f - f_0)/\text{FSR}$. In this case $z^{-1} = e^{-j2\pi\nu}$.

Assuming for example $K_r = 2/3$ (i.e. $\rho = 1/\sqrt{3}$), the filter through port transfer functions for different $\Delta\varphi$ and the corresponding pole-zero diagrams are illustrated in Fig. 2. The

upper left diagram of Fig. 2b shows that when $\Delta\varphi = 0$ the filter has three zeros in $z = -1$ and two purely imaginary complex conjugated poles. The filter transfer function (green trace in Fig. 2a) shows then two nulls at $\nu = \pm 0.5$ and a spectral behaviour similar to the symmetric interleaver presented in [18]. The 3 dB bandwidth is equal to FSR/2 and a flat passband is obtained [17]. Varying $\Delta\varphi$ from π to 0 induces a rotation of two zeros towards $z = 1$ on the unitary circle and of two poles towards the positive real axis on a circle of radius equal to ρ (see the upper part of Fig. 2b). This changes the filter transfer function reducing the filter 3 dB bandwidth from FSR/2 to its minimum (see Fig. 2a).

Instead, by varying $\Delta\varphi$ from π to 2π it is possible to increase the filter 3 dB bandwidth from FSR$/2$ to its maximum (see Fig. 2a). In this case two zeros move apart from $z = -1$ along the real axis in reciprocal positions respect to the unit circle, while two poles are rotated toward the negative real axis always on the circle of radius ρ (see the lower part of Fig. 2b). It can be shown that for any K_r, a perfectly flat passband response can be obtained only for one value of $\Delta\varphi$. For different values some in-band ripples appear but they are always below 0.3 dB, which is not too detrimental.

The through port has been considered so far. The behaviour of the cross port is complementary. The minimum (maximum) bandwidth is obtained for $\Delta\varphi = 2\pi$ ($\Delta\varphi = 0$). Inspection of equations (5), (6) and (7) also shows that for given spectral characteristics, the pole zero plot is that of the through port rotated by π.

Once the main characteristics of the filter behaviour have been introduced, in the next section its design process will be illustrated evidencing the role of the parameters that have been kept constant in this analysis.

III. Filter Design and Loss Effect

In this section the effect of the RRs coupling coefficient K_r as well as that of the losses (a and γ) will be discussed in view of the filter design. The effect of K_r will be studied first, with fixed losses. Then, once the desired value of K_r has been found, the impact of the losses on the overall performance is studied. Before illustrating the results it should also be noticed that the off-band rejection has been defined differently depending on the presence or not of sidelobes (see Fig. 2). In particular the off-band rejection is calculated with respect to the maximum of the filter sidelobes or, if no sidelobes are present, with respect to the filter absolute minimum. Moreover, the shape factor is defined as the ratio between the 1 dB and the 10 dB filter bandwidth.

This study has been performed doing extensive numerical simulations varying K_r from 0.65 to 1 (the reason of this choice will be discussed later) and $\Delta\varphi$ from 0 to 2π and calculating the corresponding values of 3 dB bandwidth, off-band rejection and shape factor. Coupler insertion loss $A = -20\log_{10}(a) = 0.06$ dB and ring resonator round trip loss $\Gamma_r = -20\log_{10}(\gamma_r) = 0.2$ dB/turn have been chosen in accordance with typical silicon-on-insulator (SOI) platform figures [19].

The results of these simulations are summarized in the maps of Fig. 3. The off-band rejection (Fig. 3a) and the shape factor (Fig. 3b) are shown as a function of K_r and of the 3 dB bandwidth normalized to the filter FSR. Level curves are drawn to help reading the different values of the colormap.

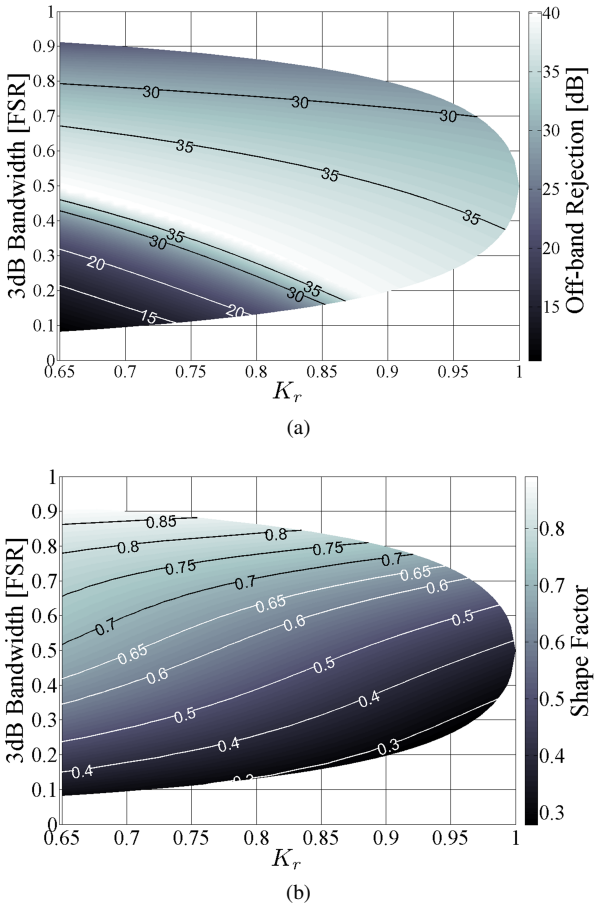

Fig. 3. (Color online) Map of the (a) filter off-band rejection and (b) shape factor (color bar and contour lines) for the 3 dB bandwidths obtained for $0 < \Delta\varphi < 2\pi$ (y axes) as a function of K_r (x axes).

The two maps show that the bandwidth tunability due to a variation of $\Delta\varphi$ from 0 to 2π reduces as the coupling coefficient increases. The limit case is represented by $K_r = 1$ where the two RRs act as pure delay lines and the filter transfer function is that of an unbalanced MZI independently of $\Delta\varphi$.

Focusing the attention on the off-band rejection, Fig. 3a shows that an overall increase of this figure of merit can be obtained increasing K_r. A trade off is thus needed to obtain both wide bandwidth tunability and a reasonable off-band rejection for all the filter configurations. In this trade off the filter shape has also to be taken into account. Increasing the RRs coupling coefficients smoothes the shape of the filter thus reducing the shape factor (see the map of Fig. 3b). An upper limit for K_r can be thus given by this parameter depending on the required performance.

These maps allow the designer to choose the value of K_r corresponding to desired performance providing at the same time a general view of the mutual effect of the parameters. A good compromise can be obtained for K_r within 0.7 and 0.8. With $K_r = 0.7$ a large bandwidth tunability, from 90% to 10% of the FSR, can be obtained with an off-band rejection always larger than 12.7 dB. With $K_r = 0.8$ an off-band rejection

larger than 20 dB for all the filter configurations is achieved but the bandwidth tunability is reduced by about 7% (i.e. $0.86 - 0.13$ FSR). With $K_r = 0.75$ an off-band rejection always larger than 20 dB can be obtained for bandwidths larger than FSR/5 maintaining an overall larger value of the shape factor. This is why we limited the lower value of K_r to 0.65 although K_r can decrease down to 0, value which corresponds to an unbalanced MZI transfer function, independently on the choice of $\Delta\varphi$.

The analysis of the maps of Fig. 3 can also be useful to define the filter robustness against fabrication tolerances. This property strongly depends on the filter working point as well as on the considered figure of merit. In the following of this section this issue will be discussed, focusing in particular on the regions of the maps within $K_r = 0.7$ and $K_r = 0.8$.

Considering first bandwidth tunability, the device shows a good robustness to fabrication tolerances. For K_r between 0.7 and 0.8, bandwidth tunability varies by about 0.7% for every 1% of K_r. However its sensitivity to a K_r variation increases as K_r increases. High values of the RRs coupling coefficient are then not the best design choice if a device with low sensitivity to fabrication tolerances is desired.

For what concerns the off-band rejection, Fig. 3a shows that larger bandwidths (> 0.5 FSR) have lower sensitivity to coupler values variations than the smaller ones (< 0.5 FSR). If, for example, $K_r = 0.75$ and a 3 dB bandwidth equal to 0.2 FSR is considered, a 5% change of K_r causes a variation of $\pm 3.5 \div 5.5$ dB in the off-band rejection from its design value (i.e. 20 dB). If this figure of merit is expected to be critical for the considered application it is then convenient to use coupling coefficients with higher values or, as it will be shown in section VI of this paper, add a control on the RRs couplers to set K_r precisely.

Regarding finally the shape factor, it can be observed from the map of Fig. 3b that in general this figure of merit varies slowly with K_r (especially for small 3 dB bandwidths) and can be thus considered less critical: the slope of the isolevel curves is in fact low almost everywhere in the map.

A fixed value of the losses ($\Gamma_r = 0.2$ dB/turn and $A = 0.06$ dB) has been considered so far. It is now interesting to see how the losses influence the filter behaviour. As a test case, we consider $K_r = 0.8$ and varying γ and thus γ_r. As expected, losses have a detrimental impact on the considered filter figures of merit and on the device insertion loss. The effect on these figures also depends on $\Delta\varphi$ as shown in Fig. 4, where three values of $\Delta\varphi$ (i.e. $0, \pi, 2\pi$) are plotted as a function of the ring round trip losses Γ_r.

Fig. 4a shows that the insertion loss increases more for the minimum bandwidth condition ($\Delta\varphi = 0$) than for the maximum one ($\Delta\varphi = 2\pi$). This can be explained noting that while f_0 matches the RRs antiresonance frequency when $\Delta\varphi = 2\pi$, it matches the RRs resonance frequency when $\Delta\varphi = 0$. In the minimum bandwidth condition the wave will then experience more round trips into the RRs and consequently a higher insertion loss as well as a higher sensitivity to Γ_r variations (larger insertion loss vs. Γ_r slope). The difference between the insertion losses of this two bandwidth conditions reaches 3 dB for values of Γ_r around 1.7 dB/turn.

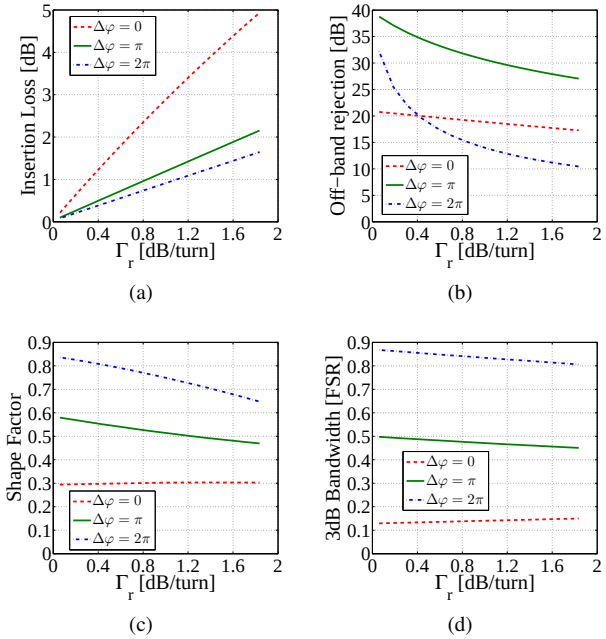

Fig. 4. (Color online) (a) Insertion loss, (b) off-band rejection, (c) shape factor and (d) 3 dB bandwidth as a function of Γ_r for $\Delta\varphi = 0$ (minimum bandwidth), $\Delta\varphi = \pi$ and $\Delta\varphi = 2\pi$ (maximum bandwidth).

Fig. 4b shows the dependence of the off-band rejection on the losses. In this case the increase in the loss factor affects more the maximum bandwidth condition ($\Delta\varphi = 2\pi$) than the minimum one ($\Delta\varphi = 0$). This comes from the method of calculation of the off-band rejection. Increasing the losses brings the zeros of the filter away from the unit circle affecting more the filter nulls than the filter sidelobes. Increasing Γ_r from 0.06 to 1.8 dB/turn the minimum bandwidth condition off-band rejection reduces from more than 20 dB to around 16 dB while the maximum bandwidth condition reduces of more than 20 dB. off-band rejection values larger than 20 dB for every filter configuration can be obtained for Γ_r lower than 0.4 dB/turn.

To increase the filter performance for large round trip loss cases it is possible to design filters with a higher value of K_r at the cost of bandwidth tunability and shape factor reduction. It should be noticed that this reduction will add to that caused by the losses. From Fig. 4c and 4d it is possible to see that the larger the round trip loss the smaller the filter shape factor (mostly for the maximum bandwidth condition) as well as the bandwidth tunability. These figures of merit show however a low sensitivity to loss variation.

It can be now pointed out that the value of Γ_r can be interpreted in two ways. A large value of Γ_r may correspond either to higher values of the ring losses with a constant L_r or a longer L_r for a given loss figure. The balance between these two constraints affects the achievable values of FSR.

IV. Group Delay and Dispersion

Before discussing the results obtained on the fabricated devices, it is convenient to briefly discuss the general filter behaviour, evidencing the effect of $\Delta\varphi$ in terms of group delay

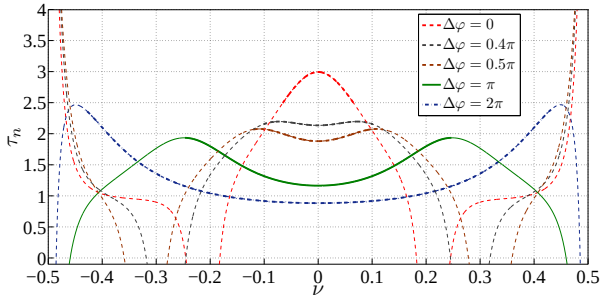

Fig. 5. (Color online) Filter through port normalized group delay τ_n for $\Delta\varphi = 0, 0.4\pi, 0.5\pi, \pi, 2\pi$, $K_r = 0.8$, $A = 0.06$ dB and $\Gamma_r = 0.2$ dB/turn.

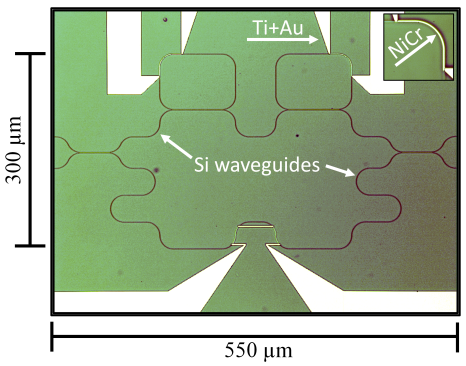

Fig. 6. (Color online) Optical microscope photograph of a fabricated filter.

and dispersion. A device with a fixed value of the coupling coefficient K_r and of the losses will be considered.

The group delay of the proposed filter varies with the amplitude of the filter transfer function. Fig. 5 shows an example of the normalized group delay characteristic τ_n of a lossy filter ($A = 0.06$ dB and $\Gamma_r = 0.2$ dB/turn) for different values of $\Delta\varphi$ and $K_r = 0.8$. The curves are thicker in the frequency range within the filter 3 dB bandwidth. The normalized group delay τ_n is related to the absolute group delay τ_g through the unit delay T (defined after (1)) by the equation $\tau_g = \tau_n T$ [17].

In the minimum bandwidth condition, at f_0, the light passes through both the resonances of the ring resonators experiencing thus the maximum group delay and high values of the dispersion at the edges of the 3 dB bandwidth. Increasing the phase shift between the RRs, the filter group delay and dispersion decrease and a minimum dispersion value in the 3 dB bandwidth (for $\Delta\varphi \in [0.4\pi, 0.5\pi]$) is found. The peaks appearing close to the frequency FSR edges are related to the presence of coupler losses. The further increase of $\Delta\varphi$ reduces then the group delay at f_0 increasing the dispersion. For $\Delta\varphi = \pi$ the group delay is minimum at f_0 and maximum at about the 3 dB bandwidth edges. In the maximum bandwidth condition ($\Delta\varphi = 2\pi$), the filter exhibits an almost constant delay in the center of the 3 dB bandwidth and a maximum dispersion close to the edges larger than that occurring for $\Delta\varphi = \pi$. The working points close to the filter maximum and minimum bandwidth conditions can be critical for signal degradation. This problem can be reduced increasing the FSR which is inversely proportional to τ_g. In general, for different values of attenuation or K_r, the described group delay evolution between minimum and maximum bandwidth conditions still hold.

After describing the general features of the filter and discussing its design issues, in the next section fabrication and measurements of some devices will be presented and discussed.

V. Device Fabrication and Performance

The filter architecture illustrated so far has been exploited to realize devices with 200, 100 and 25 GHz FSR on a silicon platform [19]. Due to the strong birefringence of SOI waveguides, device geometry depends on polarization. The fabricated structures, of which an example is shown in Fig. 6, were designed to operate with TE polarized exciting fields. The waveguides were fabricated patterning a 220 nm thick silicon layer on a 2 µm buried oxide sample of SOI using electron beam lithography and spinned and baked HSQ resist, subsequently dry-etched with an optimized process [20]. The final width of the realized waveguides is $w = 480$ nm providing single mode operations with a resulting group index of the fundamental guided quasi-TE mode $n_g \approx 4.22$. The mask was designed using constant bend radii ($= 20$ µm) and constant coupler gaps in the directional couplers of the MZI and of the RRs ($= 300$ nm). These choices also ensure respectively negligible bending losses and good couplers gap filling maintaining a compact footprint size (< 0.2 mm^2 for the device in Fig. 6). Fabricated devices were then embedded in a 900 nm thick buffer layer formed as a bilayer of spinned and baked HSQ and PECVD SiO_2. Phase shifters were then realized with a metallic NiCr/Ti-Au circuit deposited onto the waveguides and patterned by an optimized lift-off technique to exploit the thermo-optic effect [19].

An example of the realized filters thermal tuning is shown in Fig. 7a for a 25 GHz FSR filter with $K_r = 0.79$. As described in the previous analysis, the minimum bandwidth condition at the through port of the filter is reached when the two RRs resonate at the same frequencies ($\Delta\varphi = 0$) and there is a relative difference of π between the phase of the RRs and that of the MZI unloaded arm. To make the ring resonate at the same frequencies, different values of electrical power have to be dissipated over the two nominally identical RRs because of fabrication tolerances [21]. In Fig. 7b $\Delta\varphi = \varphi_{r2} - \varphi_{r1} = 0$ is in fact obtained for a power dissipated difference $\Delta P = P_{r2} - P_{r1} = -7.8$ mW, being respectively $P_{r2} = 8$ mW and $P_{r1} = 15.8$ mW the power dissipated over the two RRs. A power of 0.2 mW is dissipated over the MZI to obtain the minimum bandwidth at the through port, resulting in a total power dissipated of around 24 mW. The tuning of the bandwidth has been then obtained cooling down one of the RRs (i.e. decreasing P_{r1}) and heating up the other (i.e. increasing P_{r2}) in a push-pull confiugration, increasing consequently the value $\Delta\varphi$ up to 2π and keeping constant the total power dissipated as in [16], where the reader can find more details on the bandwidth tuning experiment. The

TABLE I
DESIGNED AND MEASURED PARAMETERS OF REALIZED DEVICES

DESIGN			MEASURED PARAMETERS											
FSR [GHz]	L_r [μm]	Foot-print [mm^2]	K_r	Γ_r [$\frac{dB}{turn}$]	FSR [GHz]	3dB bandwidth [% FSR]		IL [dB]		Off-band rejection [dB]		Shape factor		P_{tot} [mW]
								IL	EXCESS					
						U	L	U	L	U	L	U	L	
25	2841.6	< 0.6	0.79	1.77	25.1	83	16	2.2	3.1	10	15	0.68	0.31	24
100	710.4	< 0.2	0.67	0.49	99.5	89	9	0.96	1.7	20	9.5	0.83	0.3	29.5
200	355.2	< 0.2	0.75	0.26	199	87.5	11.5	0.75	0.6	19.6	15	0.81	0.31	27.5

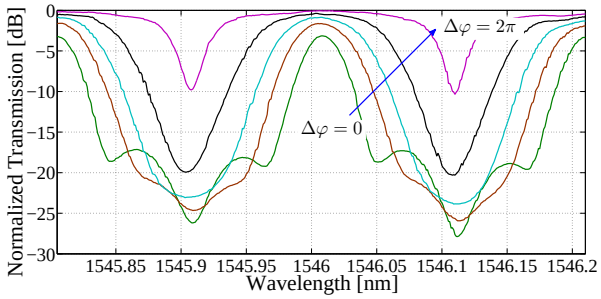

(a)

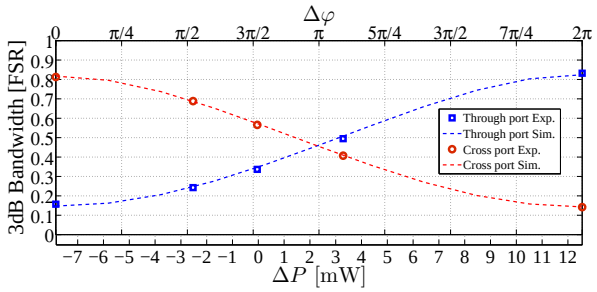

(b)

Fig. 7. (Color online) (a) Through port spectral characteristic tuning from the minimum ($\Delta\varphi = 0$) to the maximum ($\Delta\varphi = 2\pi$) bandwidth condition for a 25 GHz FSR filter with $K_r = 0.79$. (b) Measured and simulated 3 dB bandwidth values normalized to the FSR as a function of $\Delta\varphi$ (upper x axis) and of the required RRs power dissipated difference ΔP (lower x axis).

simulation results were obtained from fitted parameters where a ring loss of 1.77 dB/turn and an input/output MZI couplers value of 0.53 has been found. This deviation from the nominal 3 dB condition gives rise just to small asymmetries between the through and the cross port. Fig. 7b shows also, as expected, that the bandwidth at the cross port decreases as we increase $\Delta\varphi$.

The presented filter performance is illustrated in the first row of Tab. I, where different realized devices are compared. To simplify notation, the minimum bandwidth condition ($\Delta\varphi = 0$) is indicated with the letter L while the maximum bandwidth condition ($\Delta\varphi = 2\pi$) is indicated with the letter U. To obtain a 25 GHz FSR device, $L_r \approx 2.9$ mm must be designed. This implies an high value of Γ_r and, as formerly described, reduced performance. However the filter shows an off-band rejection always larger than 10 dB and an off-band rejection of 15 dB for the minimum bandwidth condition. The maximum bandwidth condition shows the minimum insertion loss (IL) value that is of about 2.2 dB. This value increases as the bandwidth reduces. An increase in the insertion loss (IL EXCESS) of about 3.1 dB is observed when the filter is tuned from the maximum to the minimum bandwidth condition. Bandwidth tunability is still wide, allowing to tune the device bandwidth from 21 to 4 GHz (i.e. from 83% to 16% of the FSR). For applications of the presented filter that require smaller 3 dB bandwidths (i.e longer RRs cavity lengths) such as, for example, in the microwave photonics field, the losses can be easily reduced designing RRs with larger waveguides [3], [4] increasing however the device footprint size. In this case an improvement in the performance is expected as previously discussed and illustrated in Fig. 4.

The best results are obtained, as expected, for the 200 GHz filter (third row of Tab. I) because of the reduced size of L_r. The filter 3 dB bandwidth can be tuned from 173 to 23 GHz (i.e. from 87.5% to 11.5% of the FSR) showing a low insertion loss value for all the bandwidths (maximum 1.35 for the minimum bandwidth condition). The largest improvement in terms of off-band rejection and shape factor with respect to the 25 GHz FSR filter has been obtained, in agreement with the theory, for the maximum bandwidth condition. We can also notice from the 100 GHz FSR filter (second row of Tab I) that wider bandwidth tunability (from 89% to 9% of the FSR) can be easily obtained reducing the value of K_r to 0.67. However, in this case, the off-band rejection at the minimum bandwidth condition becomes lower than 10 dB. Finally it can be noticed that the reduced number of actuators required by the proposed geometry allows for a low electrical power consumption (i.e. the total dissipated power P_{tot} is always lower than 30 mW).

The filter central wavelength $\lambda_0 = c/f_0$ can be also tuned. Adding the same positive (negative) phase φ_0 to the three phase shifters it is possible to obtain a red (blue) shift of λ_0 and thus span the whole FSR. This can be done increasing (reducing) by the same amount the power dissipated over the three phase shifters of the device. In Fig. 8 the tuning over the whole FSR has been measured for the device with 200 GHz FSR keeping the 3 dB bandwidth always around 44 GHz (i.e $\Delta\varphi$ between $\pi/2$ and $2\pi/5$). As shown in Fig. 8b, 60 mW is

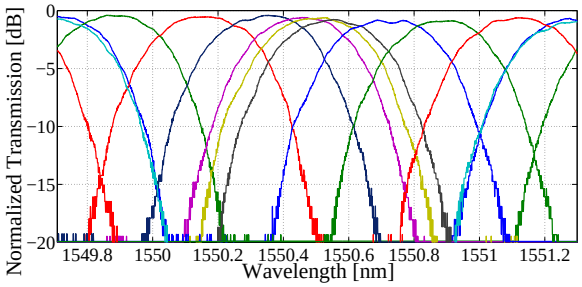

(a)

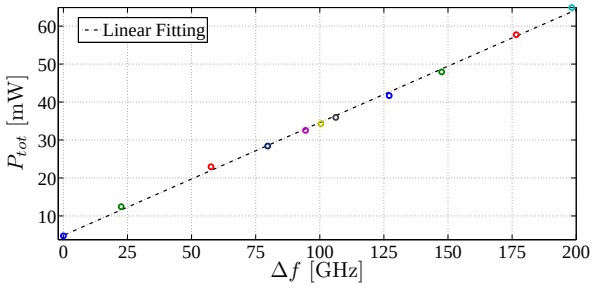

(b)

Fig. 8. (Color online) (a) Central wavelength tuning of a 44 GHz 3 dB bandwidth filter with 200 GHz FSR and (b) corresponding total power dissipated (P_{tot}) versus the frequency shift (Δf).

required to cover the whole FSR (i.e. 3.3 GHz/mW or 0.017 FSR/mW). An average of 20 mW is in fact required by the fabricated actuators to add a 2π shift to each phase shifter.

VI. Full Control via Tunable Couplers

It has been previously shown how it is possible to tailor the performance of the filter through the suitable selection of the RRs coupling coefficient during the design process. The active control of K_r would allow to have the full control over the filter functionality shown in the maps of Fig. 3 as well as to counteract the unavoidable fabrication tolerance effects, adding another degree of freedom at the device reconfigurability. This allows to better adapt the characteristics of the filter to a variation in the system requirements.

To demonstrate the possibility of obtaining this desirable feature, compact tunable couplers realized with an heater asymmetrically placed with respect to the coupler gap [22] have been designed for a filter with $K_r = 0.95$ and 25 GHz FSR without changing the geometry illustrated so far. A schematic of the proposed filter with tunable couplers is shown in Fig. 9a, where K_r is shown as a function of P_{TC}. The value of K_r can be reduced detuning the directional coupler by increasing the electrical power dissipated over the heater P_{TC}. When the two tunable couplers are switched off the filter shows bandwidth tunability from about 70% to 28% of the FSR, shape factor values between about 0.53 and 0.28 and the off-band rejection is larger than 16 dB for every filter configuration. The filter cross port minimum bandwidth condition ($\Delta\varphi = 2\pi$) for $P_{TC} = 0$ is illustrated by the dashed line in Fig. 9b. Keeping $\Delta\varphi = 2\pi$ fixed and increasing P_{TC} it is possible to reduce the minimum bandwidth from 7 to 1.8 GHz. This corresponds to a $\sim 35\%$ reduction of K_r obtained

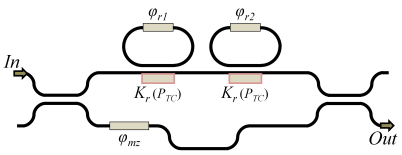

(a)

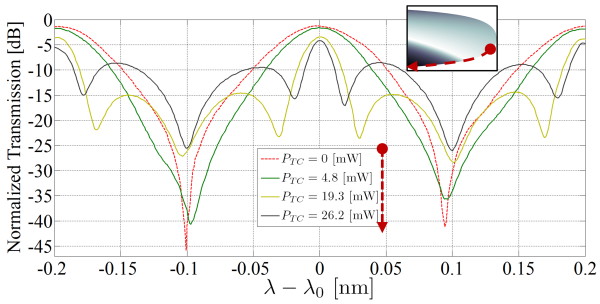

(b)

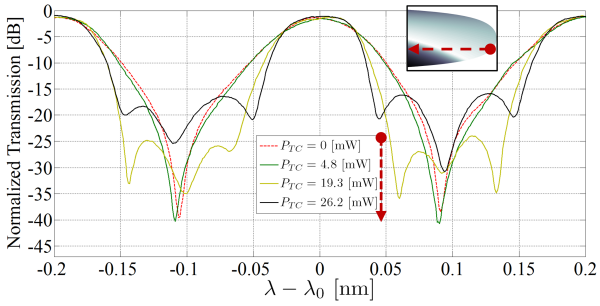

(c)

Fig. 9. (Color online) (a) Schematic diagram of the tunable filter with tunable coupling sections. The RRs coupling coefficient K_r is illustrated as a function of the dissipated power on the tunable coupler P_{TC}. (b) Filter cross port characteristic variation due to RRs couplers detuning (i.e. increasing values of P_{TC}) maintaining $\Delta\varphi = 2\pi$ (minimum bandwidth condition). (c) 7 GHz 3 dB bandwidth filter for different values of P_{TC} (and thus K_r) obtained slightly adjusting the value of $\Delta\varphi$ for each case. Insets in (b) and (c) show the off-band rejection map of Fig. 3a with the red dashed lines to evidence qualitatively the locus of the filter working points.

with a maximum $P_{TC} = 26.2$ mW. Referring to the maps of Fig. 3, this moves the filter working point along the minimum bandwidth edge (the lower one). This variation is qualitatively depicted by the red dashed line in the inset of Fig. 9b over the off-band rejection map of Fig. 3a.

Full control over the maps of Fig. 3 can be then demonstrated maintaing the same 3 dB bandwidth of the filter and changing its spectral characteristics. For example in Fig. 9c the same bandwidth has been maintained around 7 GHz (e.g. 0.28 FSR) for each configuration of the tunable couplers adjusting the value of $\Delta\varphi$. The shape factor increases from 0.28 to 0.49 while the off-band rejection decreases from 38 to 15 dB. Referring to the maps of Fig. 3 this moves the filter working point over the horizontal line defined by the value of the 3 dB bandwidth equal to 0.28 FSR. This variation is again qualitatively depicted in the inset of Fig. 9c over the off-band rejection map of Fig. 3a. The price to pay to obtain the full control over the device is an increase in the overall power consumption. This value can be reduced if lower K_r tunability is required (e.g. to counteract fabrication tolerance

effects) and asynchronous couplers are designed [22].

Up to now the filter behaviour has been discussed considering the spectral response around the central frequency. One may wonder if the filter can be used also in cases, such as DWDM, where multiple carriers are present at a time. The next section will discuss this item showing that the filter can be successfully applied also in this case allowing different operations.

VII. Multiple Bandwidths Simultaneous Tuning

As just mentioned, one of the possible application of the presented filter is in DWDM systems. In these systems one can face different needs: for example, that of filtering periodically spaced subsets of carriers (interleaver function) or of selecting a single subset of carriers. Considering the first case, the use of the 200 GHz FSR filter with 3 dB bandwidth tunable from 23 to 173 GHz, would enable the periodic selection from 1 to 7 channels from a 25 GHz spacing wavelength division multiplexing optical system. In this case the device should select all the same number of channels in the same way, no matter of the central frequency.

This is in effect possible as shown by Fig. 10a where the spectral response the 200 GHz FSR filter over 20 nm wavelength span is plotted for three bandwidth conditions ($\Delta\varphi = 0, \pi, 2\pi$). The filter bandwidth is correctly tuned for all the passbands once the required filter configuration is selected for one wavelength ($\lambda_0 = 1547.26$ nm in the considered case). This is shown more clearly in Fig. 10b where the 3 dB bandwidth at the minimum and at the maximum condition are plotted showing small variations across the considered 20 nm wavelength span. Minimum bandwidth varies of about from $+4.5$ GHz to -1.5 GHz (i.e. max 2.3% of the FSR) while the maximum bandwidth varies of about $+3$ GHz to -2.5 GHz (i.e. 1.5% of the FSR). This change occurs because of the directional couplers wavelength dependence ($\sim 6\%$ of absolute variation over the considered span). This impacts also on the off-band rejection values as shown in Fig. 10c where the value of the minimum off-band rejection varies for both the bandwidth. This value is however maintained always larger than 15.7 dB for the maximum bandwidth ($\Delta\varphi = 2\pi$, blue dashed dotted curve of Fig. 10a) and than 11 dB for the minimum one ($\Delta\varphi = 0$, red dashed curve of Fig. 10a). For the minimum bandwidth the optimum value is at the design wavelength and degrades far from it of about the same amount mainly because of the phase tuning which had been optimized for the central wavelength. The larger is the bandwidth the less it is affected by this effect. The maximum bandwidth off-band rejection varies in fact monotonically mainly because of the wavelength dependence of all the filter couplers.

In the other mentioned case, where a single passband is meant to be used to select the desired WDM channels, a much larger FSR than the one presented in this work would be required. Silicon ring resonators with a few microns bending radius and FSR with more than 2 THz [23] can be exploited for the realization of the proposed architecture. With this design choice tunability from 200 GHz to 1.8 THz is expected.

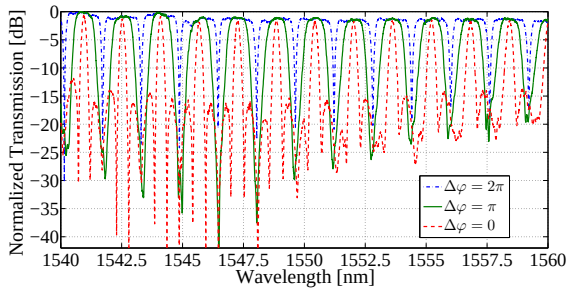

(a)

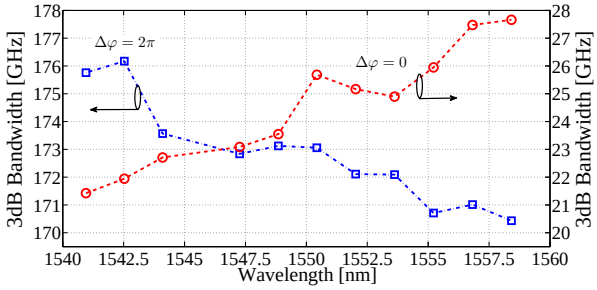

(b)

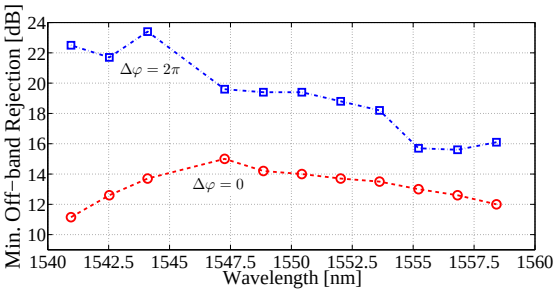

(c)

Fig. 10. (Color online) (a) 200 GHz filter spectra over 20 nm wavelength span. (b) 3 dB bandwidth and (c) off-band rejection variation over the anlayzed wavelength span for the minimum ($\Delta\varphi = 0$) and the maximum ($\Delta\varphi = 2\pi$) bandwidth condition.

The simultaneous presence of many channels may lead to high values of aggregate optical power. This requires to check if non linear effect arise with a negative impact on device behaviour. The next section will address this issue.

VIII. Impairments due to non linear effects

The dominant non linear phenomena in silicon devices are two-photon absorption (TPA) and free-carrier absorption (FCA) [24] which cause an intensity-dependent extra-loss and refractive index change. Free carrier recombination generated by TPA [25] induces a local heating of the waveguide that depends on the local optical power. This thermal effect produces an increase of the refractive index and can alter the beahviour of RRs based optical filters. The local power inside the resonators is in fact enhanced with respect to the device waveguides [26]. Different red shifts are thus induced, causing a distortion of the filter characteristic which is not simply a rigid shift. In the following it will be shown that the presented device, being based on resonators with a small value of the

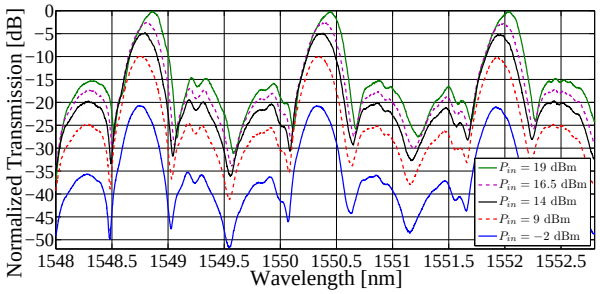

(a)

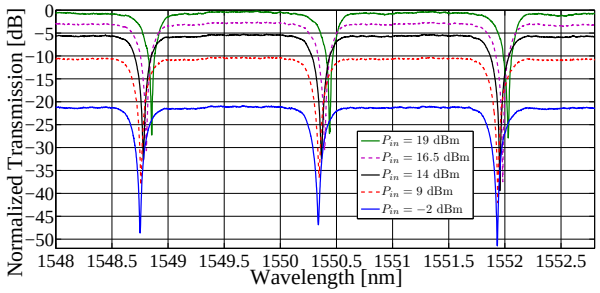

(b)

Fig. 11. (Color online) 200 GHz FSR filter (a) through port characteristic and (b) cross port characteristic for $\Delta\varphi = 0$ and increasing values of the power on chip P_{in}.

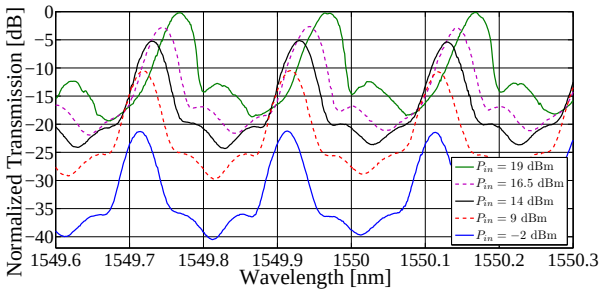

(a)

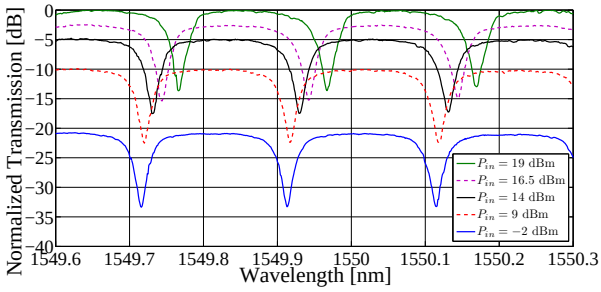

(b)

Fig. 12. (Color online) 25 GHz FSR filter (a) through port characteristic and (b) cross port characteristic for $\Delta\varphi = 0$ and increasing values of the power on chip P_{in}.

enhancement factor (i.e. strongly overcoupled resonators), is robust against TPA induced distortions.

Fig. 11 shows the spectral characteristics at the two port of the 200 GHz FSR filter of Tab. I for $\Delta\varphi = 0$, obtained through single source measurements for increasing values of the optical power on chip (P_{in}). Measuring both the through port (Fig. 11a) and the cross port characteristics (Fig. 11b) allow the evaluation of the minimum and the maximum bandwidth filter configuration with the same exact value of P_{in}. The filter RRs power enhancement factor is about 3 (i.e. the local power inside the RRs is ~ 4.8 dB higher than P_{in}).

TPA effects start to be visible for $P_{in} > 9$ dBm. The difference between the filter characteristics for $P_{in} = -2$ dBm (blue solid traces in Fig. 11) and for $P_{in} = 9$ dBm (red dashed traces in Fig. 11) are in fact negligible. For $P_{in} = 14$ dBm (black solid traces in Fig. 11), an almost rigid shift of around 30 pm occurs. This value is less than $1/5$ of the minimum filter 3 dB bandwidth and can be thus considered negligible as it appear also from Fig. 11 looking at the difference between the black solid line and the blue solid line. For $P_{in} = 19$ dBm the different shifts between the RRs resonances and the MZI waveguides slightly distort the filter response at the through port (green solid line in Fig. 11a). The cross port characteristic, due to the larger value of the bandwidth, is instead more robust and shows an almost rigid shift of around 110 pm. Moreover a maximum of just 0.22 dB of extra-loss due to the TPA has been detected.

We can then conclude that the characterized filter is just slightly affected by impairments due to TPA/FCA for values of the aggregate optical power in a WDM system up to 19 dBm. Moreover, we showed that the wider is the bandwidth the less the filter is sensitive to NL effects. It is thus reasonable to expect from devices with the same geometry but wider FSR to be even more robust. Note also that the TPA/FCA induced effect is thermal and can be easily compensated as shown in [27] if more channels and consequently higher aggregate power enters the filter.

To test the TPA/FCA effect on filters that operates on smaller bandwidths we have performed the same experiments for the 25 GHz FSR filter of Tab. I. Results are illustrated in Fig. 12 where, as before, the through port (Fig. 12a) and the cross port (Fig. 12b) characteristics are reported when $\Delta\varphi = 0$ is set. The power enhancement factor of the filter RRs is around 2 (i.e. the local power inside the RRs is ~ 3 dB higher than P_{in}).

TPA effects start to be visible as before for $P_{in} > 9$ dBm. At $P_{in} = 14$ dBm (black solid traces in Fig. 12) the characteristics of the filter are almost rigidly shifted of around 17 pm. The value of this shift is more than a half of the minimum 3 dB bandwidth and consequently cannot be considered negligible. The filter starts to be slightly distorted in the minimum bandwidth condition at $P_{in} = 16.5$ dBm (violet dashed trace in Fig. 12b) while the distortion is clearly visible for both filter configuration at $P_{in} = 19$ dBm (green solid traces in Fig. 12). With this optical power on chip a shift of about 54 pm is registered for the cross port characteristic nulls and the through port characteristic absolute maximum. The same maximum induced extra-loss as in the 200 GHz FSR device has been observed. Comparing the described results with the ones obtained for the 200 GHz FSR filter it is clear that TPA/FCA induced detrimental effects affect more filters that work with smaller bandwidths. The same induced shift becomes in fact more important as the bandwidth and the FSR decreases. The impairment is however still not dramatical for

the considered case confirming t he fi lter ro bustness an d, as previously discussed, can be easily compensated.

IX. Conclusions

In this paper we have provided an extended theoretical and experimental analysis of a compact and widely tunable silicon photonic filter w here s imple c ontrol a nd l ow power consumption are allowed by only three actuators. It has been shown that wide bandwidth tunability (from about 90% to 10% of the device FSR) can be obtained maintaining the off-band rejection always higher than 15 dB for devices with a footprint size always lower than 0.6 mm^2. Moreover the reduced number of actuators allows to obtain the bandwidth tunability with electrical power consumption always lower than 30 mW. Filter central wavelength can be also easily tuned over the whole FSR by adding a maximum of 60 mW of dissipated power. Since the filter p rincipal fi gures of me rit strongly depend on the resonator coupling coefficient and a trade off is generally needed, filters w ith c ompact t unable c ouplers has been realized maintaining the geometry unchanged. In this way the full control over the device characteristics at the cost of a reasonable increase in the power dissipated has been demonstrated. The filter c an b e s imultaneously tuned over 20 nm of the C-band and relying on strongly coupled resonators it has been shown to be robust against TPA/FCA effects. The presented characteristics make this filter suitable for reconfigurable W DM s ystem t o s elect c hannel s ubsets or to adapt its characteristic to the channel requirements.

Acknowledgment

Part of this work has been funded by the Italian PRIN 2009 project Shared Access Platform to Photonic Integrated Resources (SAPPHIRE). The authors thank the James Watt Nanofabrication Centre (JWNC) staff at Glasgow University for the support in the fabrication of the devices.

References

[1] H. L. R. Lira, C. B. Poitras, and M. Lipson, "CMOS compatible reconfigurable filter for high bandwidth non-blocking operation," *Opt. Exp.*, vol. 19, no. 21, pp. 20 115–20 121, Oct. 2011.

[2] A. Melloni and F. Morichetti, "Tunable photonic circuits: a leap toward system-on-a-chip optical integration," *SPIE Newsroom*, Jun. 2012.

[3] S. Ibrahim, N. K. Fontaine, S. S. Djordjevic, B. Guan, T. Su, S. Cheung, R. P. Scott, A. T. Pomerene, L. L. Seaford, C. M. Hill, S. Danziger, Z. Ding, K. Okamoto, and S. J. B. Yoo, "Demonstration of a fast-reconfigurable silicon CMOS optical lattice filter," *Opt. Exp.*, vol. 19, no. 14, pp. 13 245–13 256, Jul. 2011.

[4] M. S. Rasras, K.-Y. Tu, D. M. Gill, Y.-K. Chen, A. E. White, S. S. Patel, A. Pomerene, D. Carothers, J. Beattie, M. Beals, J. Michel, and L. C. Kimerling, "Demonstration of a tunable microwave-photonic notch filter using low-loss silicon ring resonators," *J. Lightw. Technol.*, vol. 27, no. 12, pp. 2105–2110, Jun. 2009.

[5] E. J. Norberg, R. S. Guzzon, J. S. Parker, L. A. Johansson, and L. A. Coldren, "Programmable Photonic Microwave Filters Monolithically Integrated in InP-InGaAsP," *J. Lightw. Technol.*, vol. 29, no. 11, pp. 1611–1619, Jun. 2011.

[6] C. R. Doerr, L. L. Buhl, L. Chen, and N. Dupuis, "Monolithic flexible-grid 1 x 2 wavelength-selective switch in silicon photonics," *J. Lightw. Technol.*, vol. 30, no. 4, pp. 473–478, Feb 2012.

[7] A. Melloni and M. Martinelli, "Synthesis of Direct-Coupled-Resonators Bandpass Filters for WDM Systems," *J. Lightw. Technol.*, vol. 20, no. 2, pp. 296–303, Feb. 2002.

[8] C. K. Madsen, "General IIR optical filter design for WDM applications using all-pass filters," *J. Lightw. Technol.*, vol. 18, no. 6, pp. 860–868, Jun. 2000.

[9] A. M. Prabhu, H. L. Liew, and V. Van, "Generalized parallel-cascaded microring networks for spectral engineering applications," *J. Opt. Soc. Am. B*, vol. 25, no. 9, pp. 1505–1514, Sep. 2008.

[10] R. Patnaik, V. Vandrasi, C. K., Madsen, A. A. Eftekhar, and A. Adibi, "Comparison of Cascade, Lattice, and Parallel Filter Architectures," *J. Lightw. Technol.*, vol. 28, no. 23, pp. 3463–3469, 2010.

[11] J. Yao and M. C. Wu, "Bandwidth-tunable add–drop filters based on micro-electro-mechanical-system actuated silicon microtoroidal resonators," *Opt. Lett.*, vol. 34, no. 17, pp. 2557–2559, Sep. 2009.

[12] L. Chen, N. Sherwood-Droz, and M. Lipson, "Compact bandwidth-tunable microring resonators," *Opt. Lett.*, vol. 32, no. 22, pp. 3361–3363, Nov. 2007.

[13] Y. Ding, M. Pu, L. Liu, J. Xu, C. Peucheret, X. Zhang, D. Huang, and H. Ou, "Bandwidth and wavelength-tunable optical bandpass filter based on silicon microring-MZI structure," *Opt. Express*, vol. 19, no. 7, pp. 6462–6470, Mar. 2011.

[14] M. S. Rasras, D. M. Gill, S. S. Patel, K.-Y. Tu, Y.-K. Chen, A. E. White, A. T. S. Pomerene, D. N. Carothers, M. J. Grove, D. K. Sparacin, J. Michel, M. A. Beals, and L. C. Kimerling, "Demonstration of a Fourth-Order Pole-Zero Optical Filter Integrated Using CMOS Processes," *J. Lightw. Technol.*, vol. 25, no. 1, pp. 87–92, Jan. 2007.

[15] P. Alipour, A. A. Eftekhar, A. H. Atabaki, Q. Li, S. Yegnanarayanan, C. K. Madsen, and A. Adibi, "Fully reconfigurable compact RF photonic filters using high-Q silicon microdisk resonators," *Opt. Express*, vol. 19, no. 17, pp. 15 899–15 907, Aug. 2011.

[16] P. Orlandi, C. Ferrari, M. J. Strain, A. Canciamilla, F. Morichetti, M. Sorel, P. Bassi, and A. Melloni, "Reconfigurable silicon filter with continuous bandwidth tunability," *Opt. Lett.*, vol. 37, no. 17, pp. 3669–3671, Sep. 2012.

[17] C. K. Madsen and J. H. Zhao, *Optical Filter Design and Analysis: A Signal Processing Approach*. New York, NY: John Wiley & Sons, Inc., 1999.

[18] K. Oda, N. Takato, H. Toba, and K. Nosu, "A wide-band guided-wave periodic multi/demultiplexer with a ring resonator for optical FDM transmission systems," *J. Lightw. Technol.*, vol. 6, no. 6, pp. 1016–1023, Jun. 1988.

[19] A. Melloni, A. Canciamilla, C. Ferrari, F. Morichetti, L. O'Faolain, T. Krauss, R. De La Rue, A. Samarelli, and M. Sorel, "Tunable delay lines in silicon photonics: Coupled resonators and photonic crystals, a comparison," *IEEE Photon. J.*, vol. 2, no. 2, pp. 181–194, Apr. 2010.

[20] M. Gnan, S. Thoms, D. S. Macintyre, R. M. De La Rue, and M. Sorel, "Fabrication of low-loss photonic wires in silicon-on-insulator using hydrogen silsesquioxane electron-beam resist," *Electron. Lett.*, vol. 44, no. 2, pp. 115–116, Jan. 2008.

[21] A. Canciamilla, M. Torregiani, C. Ferrari, F. Morichetti, R. M. De La Rue, A. Samarelli, M. Sorel, and A. Melloni, "Silicon coupled-ring resonator structures for slow light applications: potential, imapirments and ultimate limits," *J. Opt.*, vol. 12, no. 104008 (7pp.), Oct. 2010.

[22] P. Orlandi, F. Morichetti, M. J. Strain, M. Sorel, A. Melloni, and P. Bassi, "Tunable silicon photonics directional coupler driven by a transverse temperature gradient," *Opt. Lett.*, vol. 38, no. 6, pp. 863–865, Mar 2013.

[23] A. M. Prabhu, A. Tsay, Z. Han, and V. Van, "Extreme Miniaturization of Silicon Add-Drop Microring Filters for VLSI Photonics Applications," *IEEE Photon. J.*, vol. 2, no. 3, pp. 436–444, Jun. 2010.

[24] Q. Lin, O. J. Painter, and G. P. Agrawal, "Nonlinear optical phenomena in silicon waveguides: modeling and applications," *Opt. Express*, vol. 15, no. 25, pp. 16 604–16 644, Dec 2007.

[25] G. Priem, P. Dumon, W. Bogaerts, D. V. Thourhout, G. Morthier, and R. Baets, "Optical bistability and pulsating behaviour in silicon-on-insulator ring resonator structures," *Opt. Express*, vol. 13, no. 23, pp. 9623–9628, Nov. 2005.

[26] P. P. Absil, J. V. Hryniewicz, B. E. Little, P. S. Cho, R. A. Wilson, L. G. Joneckis, and P.-T. Ho, "Wavelength conversion in GaAs micro-ring resonators," *Opt. Lett.*, vol. 25, no. 8, pp. 554–556, Apr 2000.

[27] C. Ferrari, F. Morichetti, A. Canciamilla, M. Sorel, and A. Melloni, "Dynamic compensation of two-photon absorption induced distortions in silicon photonics filters," in *Lasers and Electro-Optics Europe (CLEO EUROPE/EQEC), 2011 Conference on and 12th European Quantum Electronics Conference*, May 2011, pp. 1–1.